photonics

MDPI

Article

Robust Process Parameter Optimization for Undamaged Laser Cutting of Q235B Double-Layer Narrow-Gap Steel Plates Using Random Forests

Junzhi Sun [1,†], Tianci Zhang [2,3,†], Chenglin Wang [1], Haosheng Liu [1], Chongxin Tian [4], Zhiyan Zhang [2], Shaoxia Li [4,*] and Ling Zhang [2,*]

[1] PipeChina Energy Storage Technology Co., Ltd., Shanghai 200120, China
[2] Institute of Semiconductors, Chinese Academy of Sciences, Beijing 100083, China
[3] University of Chinese Academy of Sciences, Beijing 100049, China
[4] Institute of Mechanics, Chinese Academy of Sciences, Beijing 100190, China
* Correspondence: lisx@imech.ac.cn (S.L.); zhangling@semi.ac.cn (L.Z.)
† These authors contributed equally to this work.

Abstract

To address the challenge of cutting double-layer narrow-gap steel plates without damaging the lower plate, we conducted systematic laser-cutting experiments and achieved full penetration of the upper plate without damaging the lower plate. Three cutting outcomes were defined: Unpenetrated, Undamaged, and Damaged. A random forest (RF) classifier was developed to predict the cutting outcomes, achieving 100% precision for the Undamaged class on a test split and an overall accuracy of 96.9%. The feature importance analysis indicates that laser power has an importance score of 0.230, confirming it as the most influential feature in the model. The mean regional variation in undamaged probability was computed to guide the progressive expansion of the search window for parameter optimization. The procedure was conducted with the objective of identifying the most robust parameter combinations over the global parameter space at different cutting speeds. The proposed method provides quantitative decision support for robust undamaged cutting under narrow-gap conditions.

Keywords: laser cutting; undamaged cutting; parameter optimization; random forest

1. Introduction

Downhole casings in oil and gas wells can suffer structural failures such as bending and rupture during long-term service due to geological loading and material degradation [1]. Remediation commonly requires cutting above the damaged section. In particular, the inner casing must be fully severed while the outer casing remains intact, even when the annular gap between the two casings is smaller than the wall thickness of the casing to be cut. For this operation, productivity and cut-surface quality are not the primary concerns; instead, the key requirement is reliable cutting without damaging the outer casing. Conventional methods, including explosive cutting, chemical cutting, and mechanical cutting, often involve high operational risk, environmental concerns, and low success rates [2–5]. Therefore, there is a need for an alternative technique suitable for downhole remediation. Laser cutting is a non-contact process that offers high energy density and controllability [6]. With recent advances in fiber lasers that provide improved beam quality

Check for updates

Received: 4 February 2026
Revised: 14 March 2026
Accepted: 20 March 2026
Published: 25 March 2026

Copyright: © 2026 by the authors. Licensee MDPI, Basel, Switzerland. This article is an open access article distributed under the terms and conditions of the Creative Commons Attribution (CC BY) license.

and high output power [7], laser cutting is a promising option for remote operations under harsh downhole conditions.

Q235B steel is widely used in structures and tubular components because of its favorable mechanical properties and cost effectiveness [8,9]. Most studies on laser cutting of carbon steels focus on improving cut quality and process efficiency. Xu et al. [10] improved cutting quality for complex components by studying laser cutting of four-layer stacked thin stainless-steel sheets with a 12 mm interlayer gap. Shin et al. [11,12] proposed strategies such as initial oblique cutting and stepwise speed scheduling to increase the efficiency of thick-plate cutting. For studies focusing on reducing damage during laser cutting of complex carbon steel structures, Li et al. [13] achieved high-quality cutting with limited damage through process optimization for hexagonal tube disassembly. Chagnot [14] demonstrated full penetration of a 5 mm steel plate while only slightly damaging a second plate located 40 mm away. However, ensuring high reliability and preventing damage to a nearby lower layer when the gap is smaller than the plate thickness remain challenging and are insufficiently addressed in the literature.

Cutting between plates where the gap is narrower than the plate thickness is challenging for achieving undamaged cutting. This leaves a very limited number of workable settings, making traditional trial-and-error methods ineffective. Machine learning, particularly the random forest (RF) [15–17], offers a practical route for process optimization due to its ability to handle high-dimensional nonlinear relationships [18]. Kusuma and Huang [19] compared the performance of three machine learning models, including RF, during both training and testing. The study found that RF showed the smallest discrepancy between the test and training sets, demonstrating its strong generalization ability. As an ensemble learning algorithm, RF has been widely applied in laser cutting quality prediction and process parameter importance analysis. Der et al. [20] used the RF algorithm to achieve accurate prediction of multiple quality metrics, such as laser cutting surface roughness. Nguyen [21] and the Rohman team [22–24] employed feature importance analysis to identify process parameters with a significant influence on critical metrics. This provides the foundation for subsequent research endeavors. However, previous RF-based studies focused on regression of quality metrics. Examples include kerf width and surface roughness. Only a limited number of works have used RF for laser cutting state classification. This is especially true for narrow-gap double-layer structures.

In this study, we developed a robust methodology for undamaged cutting under narrow-gap conditions using a double-layer plate configuration that mimics the relative positioning of concentric casings. Systematic experiments were first conducted to identify outcome boundaries and define the undamaged process window. An RF classifier was then trained to predict the cutting outcome and undamaged probability over the global parameter space. Finally, a robustness-oriented optimization strategy was used to determine parameter combinations that maximize undamaged cutting robustness at different cutting speeds, providing quantitative decision support for this challenging application.

2. Materials and Methods

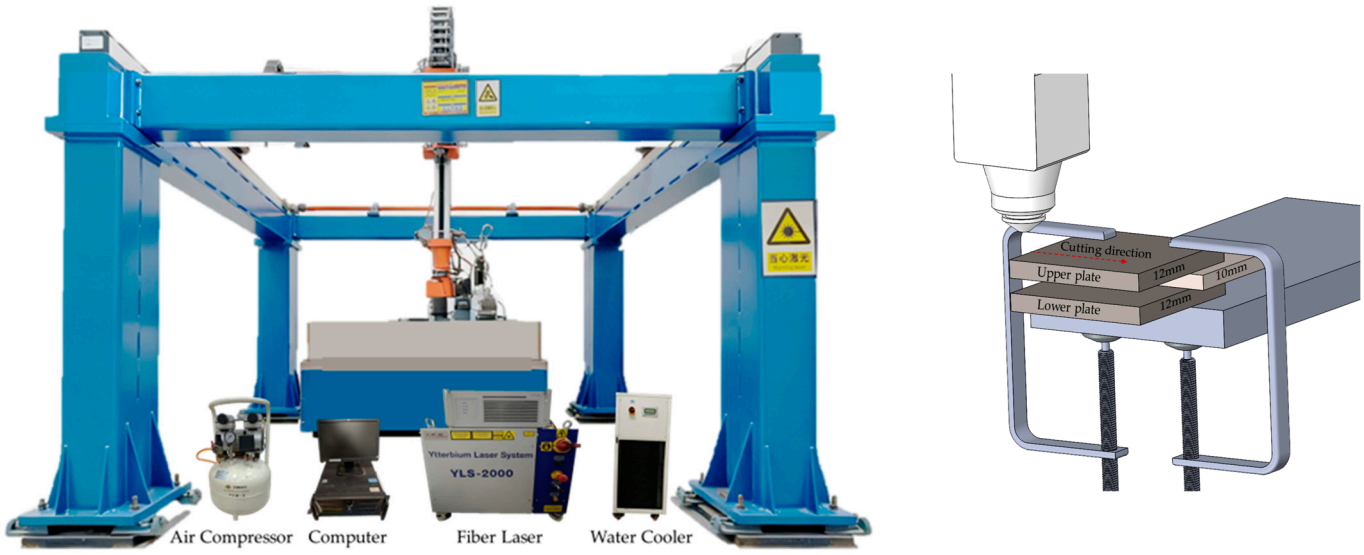
Laser cutting experiments were performed using an IPG YLS-2000 multimode continuous-wave fiber laser (wavelength: 1070 nm; beam parameter product: 4.2 mm·mrad; fiber core diameter: 100 μm). The beam was collimated with a 100 mm collimation lens and focused with a 150 mm focusing lens, producing a focused spot with an approximate diameter of 150 μm. Compressed air at 0.4 MPa was used as the assist gas.

The experimental material was Q235B steel plates measuring 100 mm × 100 mm × 12 mm, the chemical composition of which is provided in Table 1.

Table 1. Chemical composition (mass fraction) of Q235B steel.

Element	C	Si	Mn	P	S	Cr	Ni	Cu
Content (%)	0.20	0.35	1.4	0.045	0.045	0.30	0.30	0.30

Figure 1a shows the laser cutting system, and Figure 1b shows the double-layer plate structure. The engineering background of this study is the narrow-gap double-layer casing cutting scenario in oil and gas downhole remediation, where the working condition with a 12 mm wall thickness and a 10 mm annular gap is the most representative and has the most urgent engineering demand. Thus, this study focused on this core specification to carry out systematic experiments and methodological research. To mimic the relative positioning of downhole casings, two 12 mm thick Q235B plates were clamped and fixed together with a 10 mm thick spacer block using a mechanical fixture, creating a double-layer structure with a 10 mm interplate gap. The process objective was to cut completely through the upper plate without damaging the lower plate. The main experimental parameter settings were listed in Table 2. The value ranges for laser power, cutting speed, and defocus distance were established based on previous experiments. The cutting speed and defocus distance employed fixed step sizes, while a dynamic step size strategy for the laser power was applied based on the observed spark pattern during experiments. After verifying and optimizing the method for the core working condition, follow-up research will gradually expand the experimental parameter range, including systematic verification for different materials, plate thicknesses, gap sizes, as well as assist gas types and pressures, to further improve the universality of the proposed method. Unpenetrated cutting produces a splash-like spark that is easily observable. Therefore, the power step size was set to 50 W to closely approach the critical power and determine precise boundaries using fine steps. However, damage to the lower plate was difficult to assess directly from process observations. It required examination only after slag removal. To improve efficiency, the subsequent power step size was set to 150 W.



(**a**) (**b**)

Figure 1. (**a**) Laser cutting experimental setup; (**b**) Schematic of narrow-gap double-layer plate cutting.

Table 2. Parameter values and ranges.

Parameter	Min	Max	Step
Power (W)	800	2100	50; 150
Speed (mm/s)	1	3	1
Defocus (mm)	5	20	3

During the process of laser cutting, a multitude of parameters exhibit coupled effects, resulting in a certain degree of fluctuation in the final outcome, even under identical stable parameter conditions. To ensure the reliability of the Undamaged process window definition, we used a conservative recording strategy for all parameter combination outcomes. For all accumulated experimental data, if different outcomes occurred under identical parameter conditions, that parameter combination was deemed not to belong to the Undamaged class. By systematic experimentation, the power penetration threshold required for complete penetration of the upper plate and the power damage threshold to avoid damaging the lower plate were determined for combinations of defocus distance and cutting speed. These two limits define the stable process window to achieve undamaged cutting.

Positive defocus is defined as the condition where the focal plane is located above the top surface of the upper plate. In the optical configuration used here, the nozzle was fixed with the cutting head; the focal plane was located 2.5 mm below the nozzle tip, and the defocus distance was adjusted by changing the nozzle-to-workpiece stand-off distance accordingly.

The damage depth on the lower plate was measured by calculating the height difference between two focusing positions (upper surface of the lower plate and kerf bottom) using a measuring microscope. First, the focus was set on the plate's upper surface, and the height coordinate was recorded. Then, the focal plane was adjusted until the kerf bottom was clearly imaged, and the coordinate was recorded again. The actual damage depth was represented by the height difference between these two values.

Random Forest

A classification model was constructed based on the RF algorithm, the structure of which comprises an ensemble of multiple decision trees. The training process is shown in Figure 2. During training, multiple training subsets were generated from the original dataset through bootstrap sampling. When splitting nodes in each tree, a random subset of features was selected for the split, enhancing the model's diversity and generalization capabilities [25]. In the prediction phase, each decision tree independently classifies a sample. The outputs from all trees are then aggregated through a majority voting mechanism to determine the final sample class.

An RF classification model for cutting outcomes identification was constructed using all experimental data accumulated previously. To enhance the interpretability and precision of the model, features with clear physical meanings and derived features related to process parameters were implemented. Feature importance analysis was used to evaluate the contribution of each input feature to the model's cutting outcome classification, which improved the interpretability of the random forest model and provided a quantitative basis for laser cutting process parameter optimization. The random forest consists of multiple decision trees that complete classification via node splitting, where Gini impurity is adopted to measure the mixing degree of sample categories in a node: a higher value means more mixed categories, while a value of 0 indicates all samples in the node belong to the same category. The importance score of a feature is quantified by calculating the average decrease in Gini impurity when this feature is used for node splitting across all decision trees. A higher score indicates a stronger impact of the corresponding feature on

the cutting outcome classification [26]. The data were split into training (80%) and testing (20%) sets, with the stratification based on the three outcome classes to ensure the consistent proportion of samples in each class for training and testing, laying a foundation for the stability of model training [27]. Given the imbalanced ratio of Undamaged, Damaged, and Unpenetrated samples (approximately 4:1:4) in the dataset, the class weights were set to 1:4:1 for model training to mitigate the impact of sample imbalance on the classification performance. For hyperparameter tuning of the random forest classifier, the key hyperparameter (number of decision trees) was optimized by testing the model performance with the number of trees ranging from 50 to 150 at an interval of 50; the number of decision trees was finally determined to be 150 to balance the model's classification accuracy and generalization ability, while all other hyperparameters were set to the default values of the RF classifier. Confusion matrices quantify the model's classification capabilities by constructing a two-dimensional table comparing the true labels of samples with predicted counterparts. By counting correctly classified and various misclassified samples in the matrix, performance metrics such as Precision, Recall, and F1-Score were calculated. This enabled a comprehensive diagnostic assessment of the model's classification ability and overcame the limitations of relying merely on accuracy.

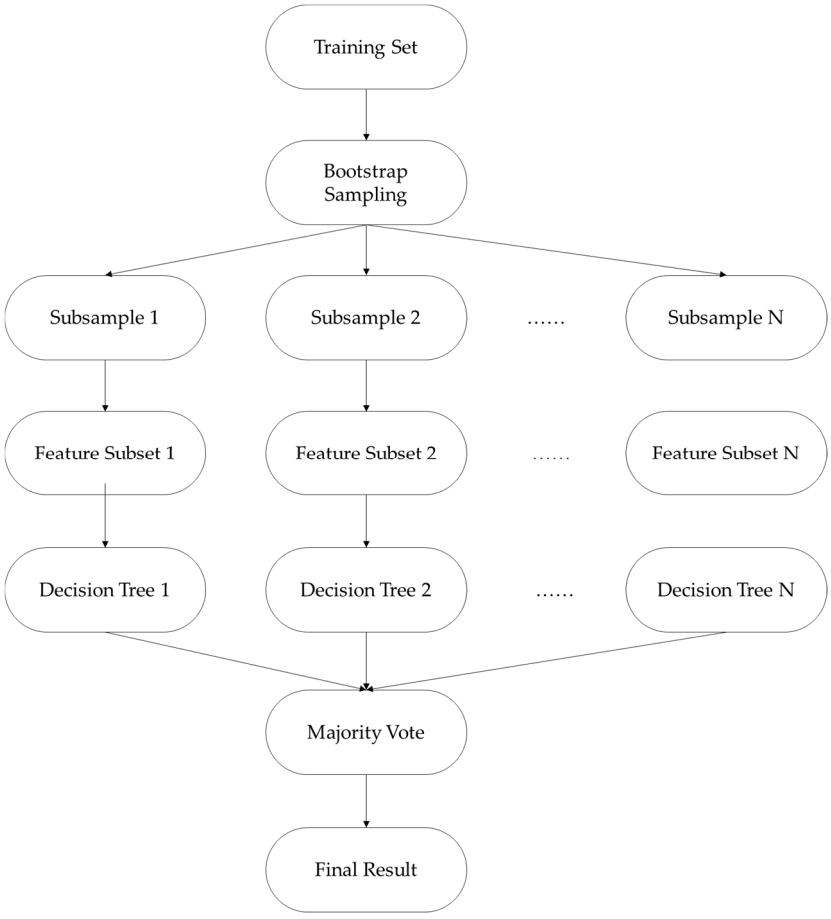


Figure 2. Random Forest classifier.

3. Results and Discussion

3.1. Cutting Morphology

In the experimental parameter range, three distinct outcomes were observed. When the power was insufficient, the upper plate remained unpenetrated, which prevented the molten material from being blown out through the bottom kerf. Under the assist gas flow, the molten material formed sparks, with the portion not blown away accumulating

on the plate surface above the kerf. This eventually solidified, forming a recast layer or adhering slag. With moderate power, the goal of undamaged cutting was achieved: the upper plate was fully penetrated, while the surface of the lower plate showed no apparent kerf after cleaning. When the power was excessive, excess laser energy damaged the lower plate, a condition defined as Damaged, resulting in a distinct kerf on its surface. Figure 3a presents the macroscopic morphology of the three outcomes Damaged, Undamaged, and Unpenetrated generated under different power levels at a defocus distance of 8 mm and a cutting speed of 2 mm/s. The corresponding laser power for each case is noted in Figure 3a. Figure 3b is a flowchart for classification of laser cutting outcomes on double-layer plates. The strategy is predicated on two fundamental decisions: firstly, confirming the penetration of the upper plate, and secondly, checking for any damage to the lower plate.

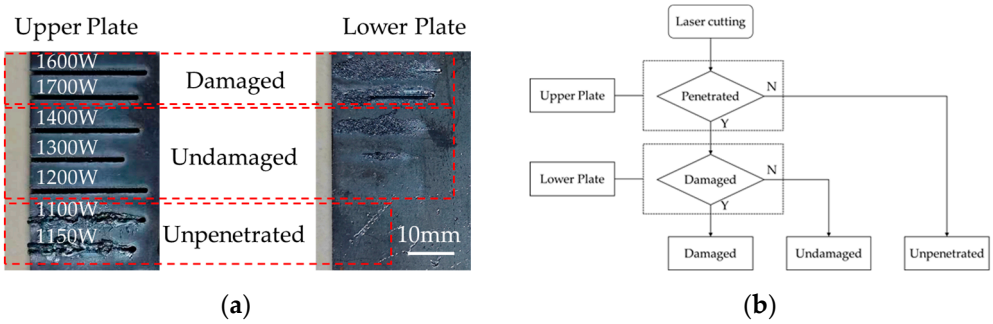


Figure 3. Three cutting outcomes. (**a**) Macroscopic morphology of the three cutting outcomes. (**b**) Flowchart for classification of laser cutting outcomes on double-layer plates.

To investigate the variation in damage morphology with defocus distance, experiments were conducted at a fixed cutting speed of 1 mm/s and a laser power of 1600 W, a power level sufficient to damage the lower plate. The cutting morphologies of both plates were investigated for defocus distances ranging from 6 mm to 20 mm with a 3.5 mm step size. The results are shown in Figure 4. As the defocus distance increased, the kerf width on the upper plate gradually increased. However, no clear trend was observed for the damage morphology on the lower plate.

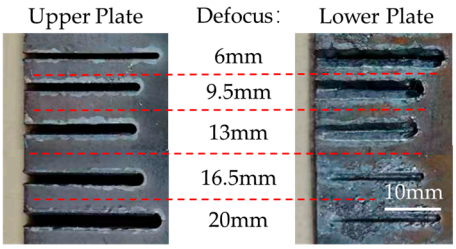


Figure 4. Damage morphology under different defocus distances.

3.2. Relationship Between Process Parameters and Damage Characteristics

The defocus distance range was expanded to systematically investigate damage on both plates under positive defocus conditions, continuing with the same cutting speed and a relatively high laser power sufficient to damage the lower plate. As shown in Figure 5, with the upper plate being fully penetrated, the kerf depth equaled the plate thickness. Under this condition, the kerf width on the upper plate increased with the defocus distance. In contrast, the damage width and depth on the lower plate showed a complex trend. The damage extent on the lower plate increased and then decreased as the positive defocus increased. Within the range of parameters, the maximum values for damage width and damage depth were found to occur at different defocus distances.

Additionally, the damage width exhibited less fluctuation over the parameter range. The maximum damage depth occurred at a defocus distance of 6 mm, although the associated damage width was narrower than that at 13 mm.

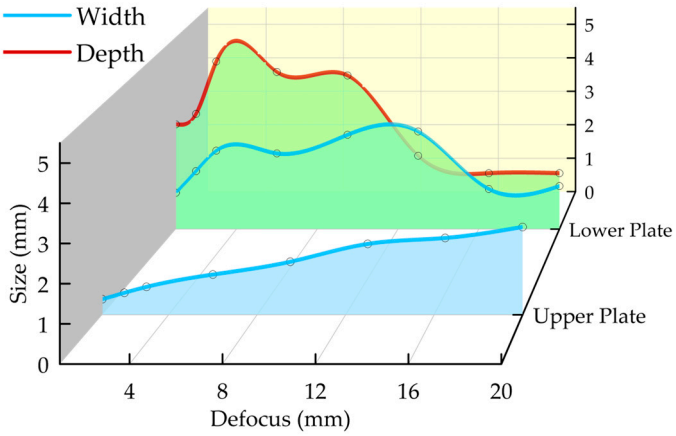


Figure 5. Influence of defocus distance on damage extent of upper and lower plates.

This phenomenon indicates competing effects among the multiple physical effects induced by defocus distance variation. Notably, changing the defocus distance directly affects two critical laser–material interaction parameters: the focused spot diameter on the material plane and the corresponding laser power density. Increasing the positive defocus distance enlarges the laser spot diameter, which in turn reduces the peak power density acting on the material. Given that the Rayleigh length of the laser cutting head was only 1.339 mm, a substantial increase in the defocus distance led to a sharp decrease in power density due to the spot expansion, which directly weakened the laser-induced thermal damage to the lower plate.

Concurrently, the enlarged spot diameter increases the kerf width in the upper plate, thereby reducing obstruction to the assist gas flow and facilitating molten material removal. However, because the nozzle is coaxially integrated into the cutting head, increasing the defocus distance necessarily alters the stand-off distance. This reduces the shear force exerted by the assist gas on the molten material, inhibiting its removal. Unremoved molten material can then continue to absorb laser energy. The kerf width in the upper plate has an approximately linear relationship with the defocus distance and exerts a complex influence on the damage depth and width of the lower plate. This complexity emerges from the combined effects of spot size expansion and the resulting non-uniform energy density distribution, as well as the correlated variation in the stand-off distance and assist gas flow field. The competing effects of the above physical processes are the direct cause of the non-monotonic trend of lower plate damage with defocus distance.

The narrow kerf of the upper plate inherently restricts gas flow, which, combined with the low assist gas pressure used in the experiment, inhibited the removal of molten material. This low-pressure condition also resulted in reduced cutting damage. To focus on the laser damage mechanism dominated by the thermal effect and reduce the influence of assist gas pressure, the lower limit of the defocus distance was set to 5 mm with a fixed step size of 3 mm for subsequent experiments.

Figure 6 shows all of the experimental outcomes. Increasing laser power leads to stepwise changes in the cutting outcomes, with clear boundaries. It was observed that there was a power penetration threshold. Energy with a value below this threshold is incapable of penetrating the upper plate. Once the power exceeds the damage threshold, irreversible changes occur. After surpassing the power damage threshold, the lower plate becomes Damaged. In this dominant power framework, cutting speed and defocus distance work

synergistically to modulate the specific values of these two critical power thresholds. Speed primarily affects the temporal integral of energy input, while defocus distance influences the effective energy absorbed by the material through a complex mechanism.

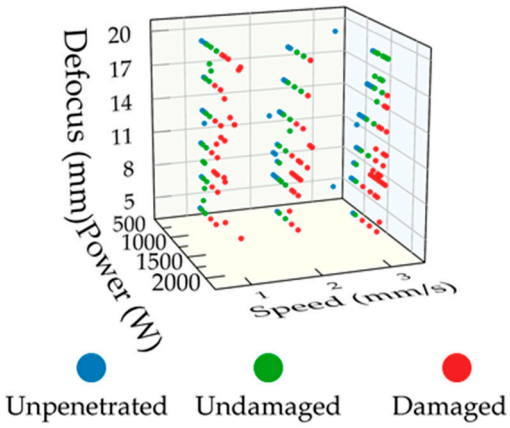


Figure 6. Cutting outcomes based on raw experimental data.

3.3. Random Forest Classification Model

To achieve stable, undamaged cutting, the focus was placed on precision. This is the proportion of true Undamaged cases among those predicted as Undamaged in the confusion matrix. It is desirable to have a higher value of precision. After clarifying the boundaries between Unpenetrated/Undamaged and Undamaged/Damaged states through process experiments, the parameter space was augmented with artificially generated data. Beginning from the lower power limit required for complete penetration of the upper plate for different defocus distances and cutting speed combinations, power was decreased in steps of 50 W, starting from the penetration threshold down to 800 W. All outcomes within this range were recorded as Unpenetrated. Similarly, starting from the critical upper power limit to avoid damaging the lower plate, the power was incremented in steps of 50 W up to 2100 W. The boundary exhibited some uncertainty because a step size of 150 W was used when determining the damage boundary threshold. All outcomes within this range were labeled as Damaged. Based on our experimental experience, the sample size could be expanded by supplementing with reliable data points. Notably, the raw experimental data overlapped with the augmented dataset, and the validity of the latter was experimentally verified in our preliminary threshold identification work, with the experimental results being fully consistent with the labeled outcomes of the augmented samples. This approach mitigated the model's tendency to misclassify Damaged or Unpenetrated cases as Undamaged, thus effectively improving the precision of the Undamaged class.

Figure 7a shows the cutting outcomes for all the parameters used to train the model, including some artificially generated data. Both the defocus distance and the cutting speed significantly influenced the boundary power values, resulting in different cutting outcomes. The cutting speed determined the energy input and affected the interaction time between the laser and the material. Higher cutting speeds corresponded to larger power boundary values between different outcomes. As the defocus distance increased, the power boundaries also increased slightly. Laser power dominantly affected irreversible transitions between cutting outcomes. Figure 7b shows the power-speed cross-section with the defocus distance fixed at 17 mm; Figure 7c displays the speed-defocus cross-section at a fixed laser power of 1600 W; and Figure 7d illustrates the power-defocus cross-section under a fixed cutting speed of 1 mm/s.

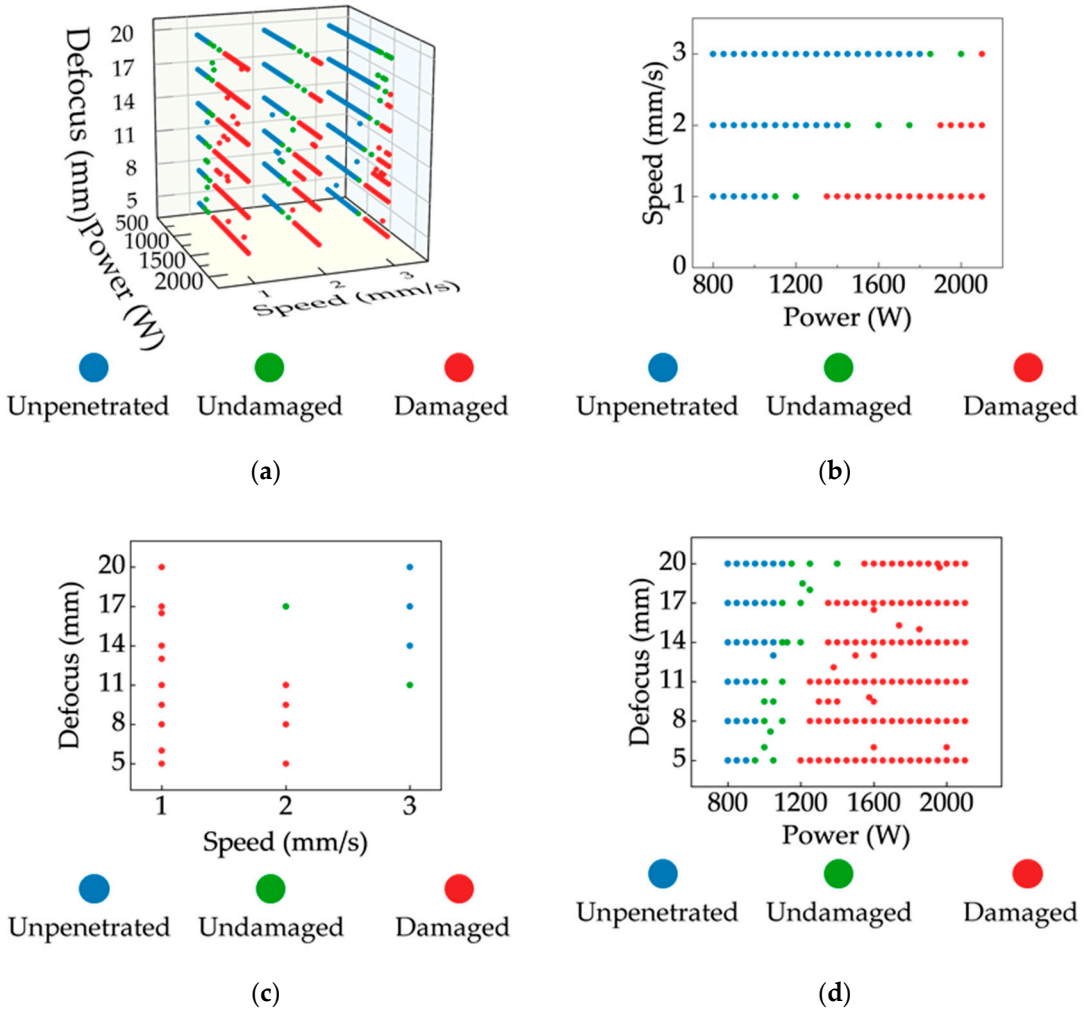


Figure 7. Cutting outcomes based on the augmented dataset. (**a**) Cutting outcomes in the global parameter space; (**b**) power-speed cross-section with fixed defocus distance 17 mm; (**c**) speed-defocus cross-section with fixed laser power 1600 W; (**d**) power-defocus cross-section with fixed cutting speed 1 mm/s.

The RF classifier model trained on these data demonstrated excellent performance. As shown in Figure 8, on an independent test set, the model achieved an overall accuracy of 96.9% (94/97). Notably, it demonstrated 100% precision for the Undamaged class, with all 8 instances correctly classified and no false positives. For the three cutting outcome classes, the detailed classification performance metrics are as follows: Unpenetrated (precision = 0.953, recall = 1.000, F1-score = 0.976), Undamaged (precision = 1.000, recall = 0.727, F1-score = 0.842), Damaged (precision = 0.978, recall = 1.000, F1-score = 0.989). All 41 Unpenetrated and 45 Damaged samples were also correctly identified, while the Undamaged class accounted for the only three misclassifications (two as Unpenetrated and one as Damaged). To verify the stability and generalization ability of the model, 5-fold stratified cross-validation was performed on the training set during the model training phase. The accuracy of each fold was 0.949, 0.935, 0.961, 0.961, and 0.974, with an average cross-validation accuracy of 0.956 ($\pm$0.013). For the Undamaged class, the average precision was 0.838 and the average recall was 0.758 across all folds. The prediction performance of the three cutting outcome classes remained stable in each fold, which verified the excellent generalization ability of the model. This model not only enabled accurate classification of cutting outcomes but also achieved effective prediction of cutting results for any combination of process parameters within the global parameter space.

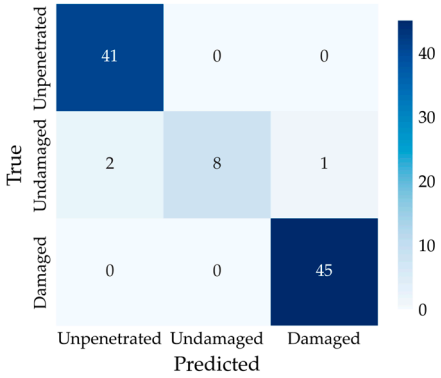


Figure 8. Confusion matrix of the RF classifier on the independent test set.

The features used to train the model consist of initial process parameters, including power, speed, and defocus distance, as well as derived features with clear physical significance. The derived features were calculated based on parameters such as the beam diameter and power on the lower surface of the upper plate. Table 3 lists the abbreviations, formulas, units, and physical meanings of the fundamental parameters and derived features. Beam diameter and beam area were used exclusively in feature calculations and were not independent features in model training. After comparing the beam information features at different locations, the beam-related features at the lower surface of the upper plate were selected for model training, as they yielded the best model performance.

Table 3. Summary of laser processing parameters and derived features.

Name	Abbreviation	Formula	Units	Physical Meaning
Fundamental Parameters				
Laser Power	Power	P	W	Laser output power
Cutting Speed	Speed	v	mm/s	Beam travel speed
Defocus Distance	Defocus	D_f	mm	Distance from the focal plane to the top surface of the upper plate
Derived Parameters (Lower Surface of Upper Plate)				
Diameter	D	$w_0\sqrt{1+((D_f+\Delta z)/z_R)^2}$	mm	Beam diameter at the lower surface of the upper plate
Area	A	$\pi\cdot(D/2)^2$	mm^2	Beam area at the lower surface of the upper plate
Power Density	PD	P/A	W/mm^2	Power per unit beam area
Linear Energy Density	LED	P/v	J/mm	Energy input per unit cutting length
Areal Energy Density	AED	$(D\cdot P)/(v\cdot A)$	J/mm^2	Energy per unit beam area over the dwell time
Energy per Point	EP	$(D\cdot P)/v$	J	Energy delivered to a point during beam passage

The importance scores of each feature, calculated via the average decrease in Gini impurity across all decision trees, are ranked in Figure 9. Power scored the highest at 0.230, making it the most critical parameter among the currently used features. The second most influential feature is Linear Energy Density (LED, defined as P/v) with a score of 0.229. Speed alone had a low importance score of 0.038, as the high importance of LED primarily stemmed from the power component, while speed acts as a key modifier. Among other beam-related features, Areal Energy Density (AED) scored the highest at 0.221.

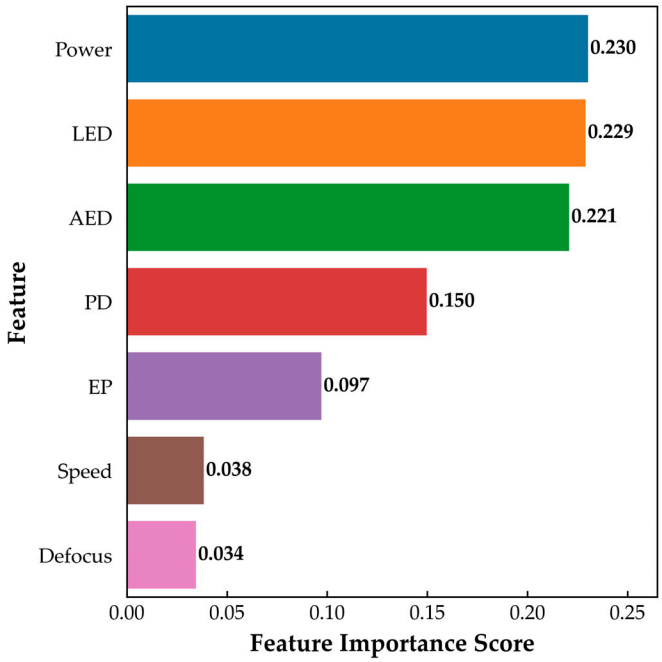


Figure 9. Feature importance scores based on mean decrease in Gini impurity.

To quantitatively disassemble the influencing factors of the non-monotonic trend of lower plate damage with defocus distance, we conducted a quantitative contribution analysis based on SHapley Additive exPlanations (SHAP) values for the Damaged class [28,29]. The SHAP beeswarm plot (Figure 10) shows the distribution of SHAP values for each feature, where the x-axis represents the SHAP value (positive values increase the probability of damage, negative values decrease the probability of damage), and the color represents the feature value from low (blue) to high (red). It can be seen that AED, Power, and LED are the three most influential features for damage probability, with high feature values corresponding to positive SHAP values, indicating that the increase in these three parameters will significantly promote the occurrence of damage. For the Defocus feature, low defocus values correspond to positive SHAP values that promote damage, while high defocus values correspond to negative SHAP values that inhibit damage, confirming that its influence on damage probability is non-monotonic, which is consistent with the experimental phenomenon.

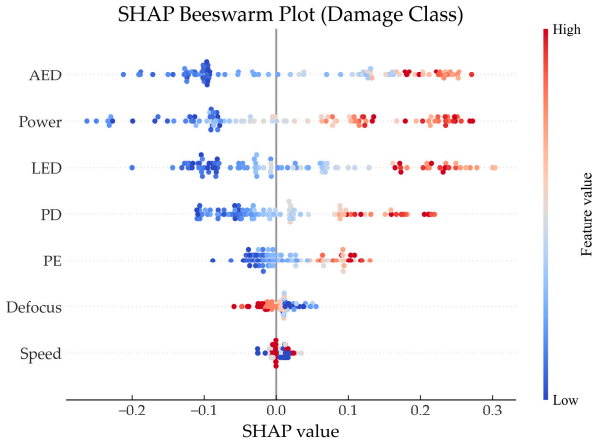


Figure 10. SHAP Beeswarm Plot for the Damaged class.

The variation trend of the damaged probability with defocus distance at a fixed cutting speed of 1 mm/s and a laser power of 1600 W is shown in Figure 11, which reproduces

the non-monotonic change in damage with defocus distance observed in the experiment and verifies the reliability of the model for describing this phenomenon. Figure 12 shows the variation trend of SHAP contribution values of core parameters with defocus distance increasing from 5 mm to 20 mm, at a fixed cutting speed of 1 mm/s and a laser power of 1600 W. With the increase in defocus distance, the SHAP contribution of Power Density (PD) gradually changes from positive to negative, indicating that its effect on damage probability shifts from promotion to inhibition, while the SHAP contribution of LED remains positive and increases continuously, with its promoting effect on damage probability gradually enhanced. The SHAP contribution of AED is always positive throughout the range of defocus distance, making it the most core feature affecting the damage probability. The competitive relationship between the opposite trends of PD and LED is the root cause for the absence of a clear monotonic trend in lower plate damage with defocus distance.

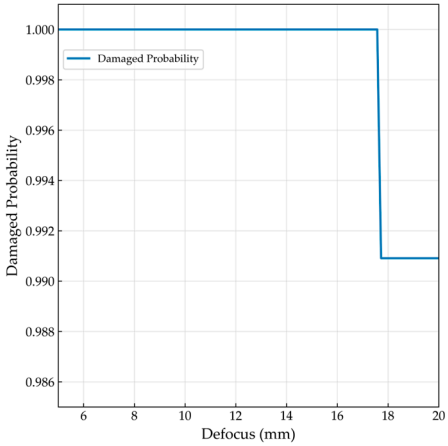


Figure 11. Variation in Damaged Probability with Defocus Distance at Fixed Cutting Speed of 1 mm/s and Laser Power of 1600 W.

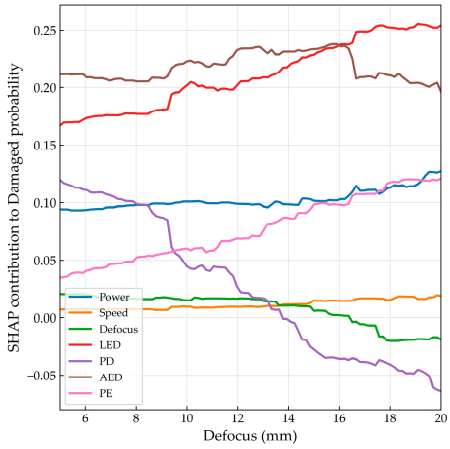


Figure 12. Variation in Features' SHAP Contribution Values with Defocus Distance over 5–20 mm at Fixed Cutting Speed of 1 mm/s and Laser Power of 1600 W.

The power and defocus distances were divided into 500 equal intervals to predict the cutting results and undamaged probability values for all grid points in the parameter space at different speeds. Figure 13a–c illustrate the predicted cutting results at speeds of 1 mm/s, 2 mm/s, and 3 mm/s, respectively. In these figures, triangles, circles, and squares represent the actual experimental data points for Unpenetrated, Undamaged, and Damaged results, respectively, in each case. The blue, green, and red areas correspond to the three predicted result categories across the parameter space. Some parameter points that were actually from the Undamaged class were incorrectly predicted as Damaged or Unpenetrated, as

indicated by the red circles in Figure 13 a–c. These misclassifications occurred in specific parameter regions and slightly affected the overall model performance. Figure 13d–f show the predicted undamaged probabilities across the global parameter space at each speed. Due to the limited number of effective undamaged process parameters, the predicted undamaged probability values were lower at the highest speed than at other speeds.

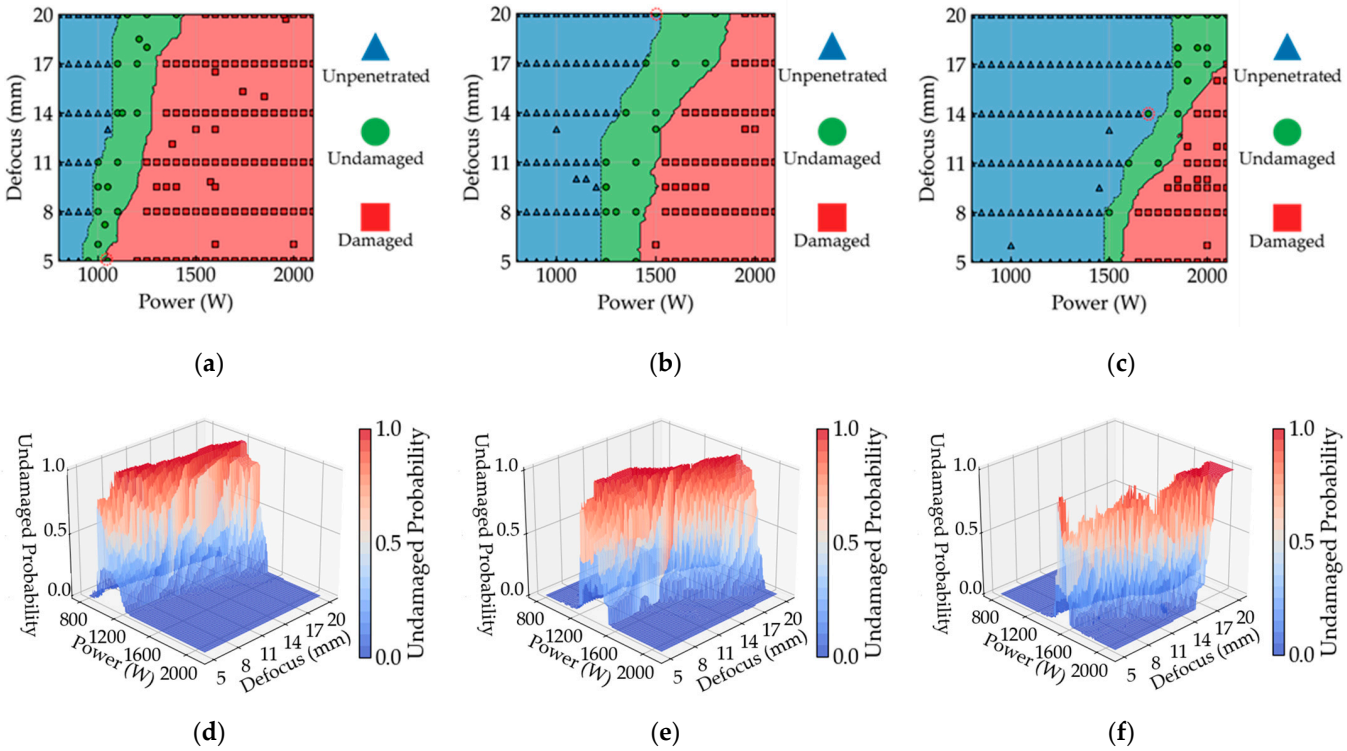


Figure 13. Predictions in the global parameter space at different cutting speeds. (**a**) Classification at 1 mm/s; (**b**) Classification at 2 mm/s; (**c**) Classification at 3 mm/s; (**d**) Undamaged probability at 1 mm/s; (**e**) Undamaged probability at 2 mm/s; (**f**) Undamaged probability at 3 mm/s.

To quantify the stability of the model's process window boundary prediction, the mean and standard deviation of the penetration threshold and damage threshold under different cutting speeds and defocus distances were calculated based on the 5-fold cross-validation results. The results showed that the average standard deviation of the penetration threshold was 20.8 W, and the average standard deviation of the damage threshold was 20.0 W. The ±1 standard deviation fluctuation intervals of the two thresholds at different cutting speeds are shown in Figure 14, which quantifies the stability of the model's prediction of the undamaged process window boundary.

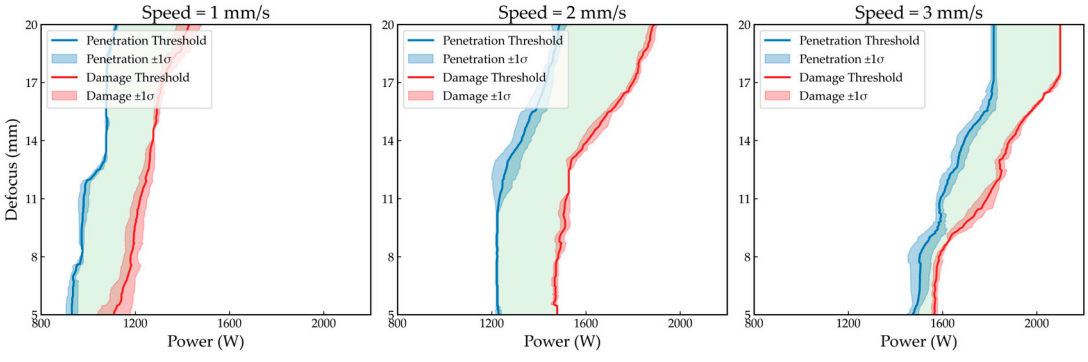


Figure 14. Fluctuation intervals of penetration threshold and damage threshold at different cutting speeds.

The search for maximum undamaged probability points began with a scan of the global parameter space. When multiple points shared the same maximum Undamaged probability, all candidate points were recorded, and the regional stability scores centered on each candidate point were compared. This score was obtained by calculating the regional average probability variation from each point within the region to its center point. A lower regional score indicates higher robustness of the candidate point.

The defocus distance window of the search region was fixed at 1 mm, with consideration given to practical fluctuations. To efficiently identify the optimal parameters, the initial power window was set to 40 W and was gradually increased in 5 W steps. The expansion ceased when a unique minimum value of the average Undamaged probability variation was identified within the region, centered on a candidate parameter point, which ensured that only one most robust parameter was identified. This approach ensures optimal parameter identification while preventing substantial interference from other data due to an excessively large search window.

The final region sizes vary depending on the processing speed. At speeds of 1 mm/s and 2 mm/s, the final window sizes are 55 W and 60 W, respectively. At a speed of 3 mm/s, the size of the window is 240 W, with its limitations primarily being the result of the upper power boundary and the absence of a complete damage threshold. The optimal robust parameters, marked by circles in Figure 15a–c, are as follows: a laser power of 1175 W with a defocus distance of 16.5 mm; a laser power of 1290 W with a defocus distance of 9.8 mm; and a laser power of 2100 W with a defocus distance of 20 mm. The most robust parameters for each speed are shown in Figure 15d. To quantify the error range of the optimal parameters under practical parameter fluctuations, the fluctuation tolerance of each optimal robust parameter set was calculated, defined as the maximum parameter variation range where the predicted undamaged probability was maintained above 0.95. For the optimal parameter at 1 mm/s (Power = 1175 W, Defocus = 16.5 mm, undamaged probability = 1.0000), the fluctuation tolerance is ±60 W for laser power and ±2.7 mm for defocus distance. For the optimal parameter at 2 mm/s (Power = 1290 W, Defocus = 9.8 mm, undamaged probability = 1.0000), the fluctuation tolerance is ±60 W for laser power and ±1.6 mm for defocus distance. For the optimal parameter at 3 mm/s (Power = 2100 W, Defocus = 20.0 mm, undamaged probability = 1.0000), the fluctuation tolerance is ±235 W for laser power and ±1.8 mm for defocus distance. This result provides a quantitative reference for parameter adjustment in practical engineering applications, ensuring the stability of undamaged cutting under parameter fluctuations in field operations.

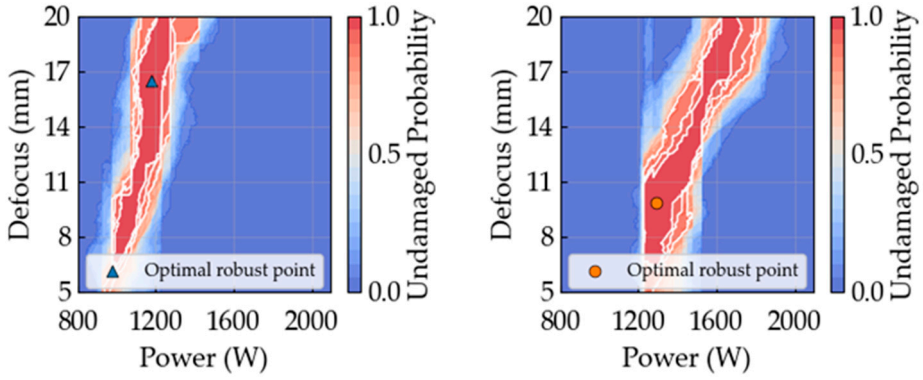
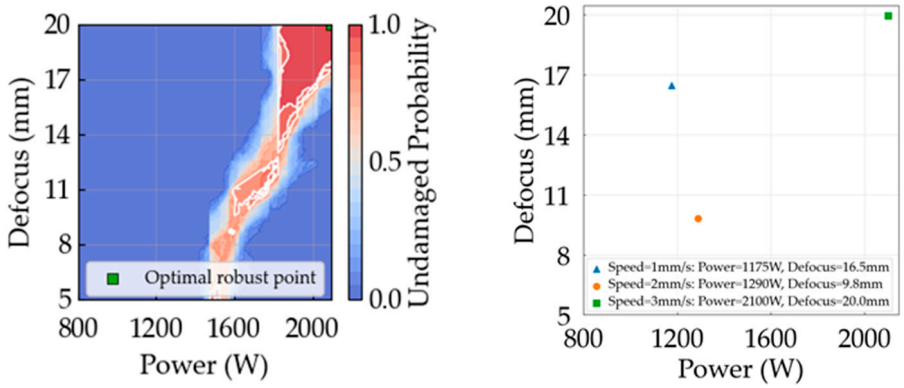


Figure 15. *Cont.*

https://doi.org/10.3390/photonics13040315



(**c**) (**d**)

Figure 15. Predictions in the global parameter space. (**a**) Optimal robust parameters at 1 mm/s; (**b**) Optimal robust parameters at 2 mm/s; (**c**) Optimal robust parameters at 3 mm/s; (**d**) Optimal robust parameter summary.

4. Conclusions

In this study, we conducted a systematic experimental investigation of laser cutting on narrow-gap, double-layer Q235B steel plates under normal temperature and pressure conditions, achieving full penetration of the upper plate without damaging the lower plate. This work establishes the fundamental methodological basis for the subsequent engineering application of this technology in actual downhole operations. An RF classifier was established to predict cutting outcomes and undamaged probability over the global parameter space, enabling robustness-oriented parameter selection. The main conclusions are as follows: Within the investigated ranges, three cutting outcomes were observed: Unpenetrated, Undamaged, and Damaged. Laser power primarily governed the transitions among these outcomes, while cutting speed and defocus distance shifted the corresponding threshold power levels. The constructed Random Forest Classification Model achieved a precision of 100% for the Undamaged class on an independent test set and an overall accuracy of 96.9%. The feature importance analysis showed that laser power has an importance score of 0.230, further confirming it as the most influential feature in the model; A robustness optimization strategy was proposed based on the undamaged probability distribution. By combining a global search with a regional robustness metric (mean variation in undamaged probability within a neighborhood) and progressive window expansion, the method identified a unique set of most robust parameters at each cutting speed. These parameter sets provide quantitative decision support for undamaged cutting under narrow-gap conditions and are expected to better tolerate practical parameter fluctuations in actual downhole operations. Limited by the existing experimental conditions, we currently lack special simulation and experimental devices suitable for the high-temperature and high-pressure environment of downhole operations. For actual downhole working conditions including high temperature, high pressure, and complex media, follow-up research will gradually improve the relevant environmental simulation and numerical simulation work, establish a parameter correction model combined with the environmental characteristics of downhole working conditions, and form a supporting engineering implementation scheme to promote the field application of this method.

Author Contributions: Conceptualization, J.S. and T.Z.; methodology, C.T.; software, C.W.; validation, H.L., S.L. and L.Z.; formal analysis, Z.Z.; investigation, J.S.; resources, C.W.; data curation, H.L.; writing—original draft preparation, T.Z.; writing—review and editing, S.L. and L.Z.; visualization, C.T.; supervision, L.Z.; project administration, Z.Z.; funding acquisition, S.L. and L.Z. All authors have read and agreed to the published version of the manuscript.

Funding: This research received no external funding.

Institutional Review Board Statement: Not applicable.

Informed Consent Statement: Not applicable.

Data Availability Statement: The original contributions presented in this study are included in the article. Further inquiries can be directed to the corresponding authors.

Conflicts of Interest: Junzhi Sun, Chenlin Wang and Haosheng Liu are employees of PipeChina Energy Storage Technology Co. All the authors declare no conflicts of interest.

Abbreviations

The following abbreviations are used in this manuscript:

P	Laser Power (W)
v	Cutting Speed (mm/s)
D_f	Defocus Distance (mm)
w_0	Beam waist diameter at focal point (mm)
z_R	Rayleigh length (mm)
Δz	Upper plate thickness (mm)
D	Beam diameter at the lower surface of the upper plate (mm)
A	Beam area at lower surface of upper plate (mm^2)

References

1. Zachary, C.; Bello, O.; Teodoriu, C. Calculation and Prediction of Casing Collapse Strength Based on a New Yield Strength Acquisition Method. *J. Nat. Gas Sci. Eng.* **2021**, *95*, 104149. [CrossRef]
2. Cai, C.; Zeng, L.; Liu, J.; Fan, K.; Cao, W.; Zhou, S.; Zeng, X. Development Status and Trend of Downhole Cutting Technology for Oil and Gas Wells. *J. Xi'an Shiyou Univ.* **2024**, *39*, 89–96.
3. Zhang, P.; Wang, C.; Wu, T. Application of Electroplated Diamond Cutting Tools in Cutting Multilayer Casings in Underground Coal Mines. *Superhard Mater. Eng.* **2018**, *30*, 38–42.
4. Liu, H.; Ye, H.; Tian, M.; Wu, G.; Xiao, B. Application of the mechanical cutting technology for coiled tubing in Yong 25-11 well. *Complex Hydrocarb. Reserv.* **2014**, *7*, 79–81. [CrossRef]
5. Otten, H.; Connon, B.; McKay, A.; Kirsanov, K.; McGillivray, M. Electric-Line Pipe-Cutting Operation Optimizes Completion Removal, Offshore Russia. In *Proceedings of the SPE/ICoTA Coiled Tubing & Well Intervention Conference & Exhibition, The Woodlands, TX, USA, 26–27 March 2013*; SPE: Richardson, TX, USA; p. SPE-163890-MS.
6. Niu, J.; Liu, W.; Li, J.X.; Pang, X.; Liu, Y.; Zhang, C.; Yue, K.; Zhou, Y.; Xu, F.; Li, X.; et al. Machining Water through Laser Cutting of Nanoparticle-Encased Water Pancakes. *Nat. Commun.* **2023**, *14*, 3853. [CrossRef]
7. Ding, X.; Zeng, L.; Wang, L.; Wu, H.; Wang, P.; Zhang, H.; Wang, X.; Ning, Y.; Xi, F.; Xu, X. 2 × 4.5 kW Bidirectional Output near-Single-Mode Quasi-Continuous Wave Monolithic Fiber Laser. *Sci. Rep.* **2023**, *13*, 21218. [CrossRef]
8. Qiu, F.; Bai, Y.; Qu, D.; Shan, G.; Han, L.; Chen, W. Quantitative Characterization of Q235B Steel Electrochemical Corrosion by Acoustic Emission. *Int. J. Press. Vessel. Pip.* **2022**, *199*, 104686. [CrossRef]
9. Yang, Q.; Xiong, Y.; Huang, Y.; Cheng, J.; Lou, D.; Chen, L.; Li, Q.; Liu, D. Nanosecond Laser Passivation Mechanism of Q235B Carbon Steel Surface. *J. Mater. Eng. Perform.* **2025**, *34*, 2371–2379. [CrossRef]
10. Xu, L.; Wang, C.; Yan, F.; Hu, Z.; Zhang, W. Improved Surface Quality and Microstructure Regulation in High Power Fiber Laser Cutting of Stainless Steel Grid Plates. *Materials* **2024**, *17*, 5959. [CrossRef] [PubMed]
11. Shin, J.S.; Oh, S.Y.; Park, S.-K.; Park, H.; Lee, J. Improved Underwater Laser Cutting of Thick Steel Plates through Initial Oblique Cutting. *Opt. Laser Technol.* **2021**, *141*, 107120. [CrossRef]
12. Seon, S.; Shin, J.S.; Oh, S.Y.; Park, H.; Chung, C.-M.; Kim, T.-S.; Lee, L.; Lee, J. Improvement of Cutting Performance for Thick Stainless Steel Plates by Step-like Cutting Speed Increase in High-Power Fiber Laser Cutting. *Opt. Laser Technol.* **2018**, *103*, 311–317. [CrossRef]
13. Li, T.; Mo, Z.; Zhou, J.; Chen, Q.; Cao, Z.; Guo, J.; Yang, Z.; Tang, C.; Li, W.; Ming, Y.; et al. Experimental Study on the Laser Cutting Process of the Stainless Steel Hexagonal Tube of Fast Reactor Simulate Assembly. *Nucl. Eng. Des.* **2025**, *432*, 113788. [CrossRef]
14. Chagnot, C.; De Dinechin, G.; Canneau, G. Cutting Performances with New Industrial Continuous Wave ND:YAG High Power Lasers. *Nucl. Eng. Des.* **2010**, *240*, 2604–2613. [CrossRef]

15. Breiman, L. Random Forests. *Mach. Learn.* **2001**, *45*, 5–32. [CrossRef]
16. Khan, I.A.; Birkhofer, H.; Kunz, D.; Lukas, D.; Ploshikhin, V. A Random Forest Classifier for Anomaly Detection in Laser-Powder Bed Fusion Using Optical Monitoring. *Materials* **2023**, *16*, 6470. [CrossRef]
17. Maia, L.S.P.; Barroso, D.A.; Silveira, A.B.; Oliveira, W.F.; Galembeck, A.; Fernandes, C.A.R.; Bandeira, D.G.C.; Cluzel, B.; Alexandria, A.R.; Guimarães, G.F. Inverse Design of Plasmonic Nanostructures Using Machine Learning for Optimized Prediction of Physical Parameters. *Photonics* **2025**, *12*, 572. [CrossRef]
18. Du, Q.; Wang, Z.; Huang, P.; Zhai, Y.; Yang, X.; Ma, S. Remote Sensing Monitoring of Grassland Locust Density Based on Machine Learning. *Sensors* **2024**, *24*, 3121. [CrossRef]
19. Kusuma, A.I.; Huang, Y.-M. Performance Comparison of Machine Learning Models for Kerf Width Prediction in Pulsed Laser Cutting. *Int. J. Adv. Manuf. Technol.* **2022**, *123*, 2703–2718. [CrossRef]
20. Der, O. Multi-Output Prediction and Optimization of CO_2 Laser Cutting Quality in FFF-Printed ASA Thermoplastics Using Machine Learning Approaches. *Polymers* **2025**, *17*, 1910. [CrossRef] [PubMed]
21. Nguyen, T.H.; Lin, C.-K.; Tung, P.-C.; Nguyen-Van, C.; Ho, J.-R. An Extreme Learning Machine for Predicting Kerf Waviness and Heat Affected Zone in Pulsed Laser Cutting of Thin Non-Oriented Silicon Steel. *Opt. Lasers Eng.* **2020**, *134*, 106244. [CrossRef]
22. Rohman, M.N.; Ho, J.-R.; Tung, P.-C.; Lin, C.-T.; Lin, C.-K. Prediction and Optimization of Dross Formation in Laser Cutting of Electrical Steel Sheet in Different Environments. *J. Mater. Res. Technol.* **2022**, *18*, 1977–1990. [CrossRef]
23. Rohman, M.N.; Ho, J.-R.; Tung, P.-C.; Tsui, H.-P.; Lin, C.-K. Prediction and Optimization of Geometrical Quality for Pulsed Laser Cutting of Non-Oriented Electrical Steel Sheet. *Opt. Laser Technol.* **2022**, *149*, 107847. [CrossRef]
24. Rohman, M.N.; Ho, J.-R.; Lin, C.-T.; Tung, P.-C.; Lin, C.-K. Predicting and Enhancing the Multiple Output Qualities in Curved Laser Cutting of Thin Electrical Steel Sheets Using an Artificial Intelligence Approach. *Mathematics* **2024**, *12*, 937. [CrossRef]
25. Parmar, A.; Katariya, R.; Patel, V. A Review on Random Forest: An Ensemble Classifier. In *International Conference on Intelligent Data Communication Technologies and Internet of Things (ICICI) 2018*; Hemanth, J., Fernando, X., Lafata, P., Baig, Z., Eds.; Lecture Notes on Data Engineering and Communications Technologies; Springer International Publishing: Cham, Switzerland, 2019; Volume 26, pp. 758–763; ISBN 978-3-030-03145-9.
26. Shao, J.; Liu, Y.; Du, X.; Xie, T. Adaptive Modulation Scheme for Soft-Switching Hybrid FSO/RF Links Based on Machine Learning. *Photonics* **2024**, *11*, 404. [CrossRef]
27. Steege, T.; Bernard, G.; Darm, P.; Kunze, T.; Lasagni, A.F. Prediction of Surface Roughness in Functional Laser Surface Texturing Utilizing Machine Learning. *Photonics* **2023**, *10*, 361. [CrossRef]
28. Lundberg, S.M.; Lee, S.-I. A Unified Approach to Interpreting Model Predictions. *arXiv* **2017**, arXiv:1705.07874. [CrossRef]
29. Barile, C.; Carone, S.; Casavola, C.; Pappalettera, G. Quantification of the Influence of Laser Shock Peening Parameters on Residual Stresses in Thick AA 7050 Specimens: An Experimental and Explainable Machine Learning-Based Approach. *Mech. Mater.* **2026**, *212*, 105536. [CrossRef]

Disclaimer/Publisher's Note: The statements, opinions and data contained in all publications are solely those of the individual author(s) and contributor(s) and not of MDPI and/or the editor(s). MDPI and/or the editor(s) disclaim responsibility for any injury to people or property resulting from any ideas, methods, instructions or products referred to in the content.